

Article

Petrogenesis of Ore-Hosting Diorite in the Zaorendao Gold Deposit at the Tongren-Xiahe-Hezuo Polymetallic District, West Qinling, China

Zong-Yang Gou^{1,2}, Hao-Cheng Yu^{1,2}, Kun-Feng Qiu^{1,2,3,*} , Jian-Zhen Geng¹, Ming-Qian Wu^{1,4} , Yong-Gang Wang⁵, Ming-Hai Yu⁶ and Jun Li¹

¹ State Key Laboratory of Geological Processes and Mineral Resources, and School of Earth Science and Resources, China University of Geosciences, Beijing 100083, China; zongygou@cugb.edu.cn (Z.-Y.G.); haochengyu@cugb.edu.cn (H.-C.Y.); mumu1270@163.com (J.-Z.G.); aria.wu1990@gmail.com (M.-Q.W.); 2001170100@cugb.edu.cn (J.L.)

² Key Laboratory of Mineral Resources, Institute of Geology and Geophysics, Chinese Academy of Sciences, Beijing 100029, China

³ Department of Geology and Geological Engineering, Colorado School of Mines, Golden, CO 80401, USA

⁴ Department of Earth and Environmental Sciences, University of Windsor, Windsor, ON N9B 3P4, Canada

⁵ Guangxi Geological Exploration Institute of CCGMB, Nanning 530001, China; Yonggwang@163.com

⁶ Zhaojin Ming Industry co., LTD, Zhaoyuan 265400, China; minghyu@126.com

* Correspondence: kunfengqiu@cugb.edu.cn; Tel.: +86-10-82321383

Received: 15 December 2018; Accepted: 24 January 2019; Published: 28 January 2019



Abstract: The newly discovered Zaorendao gold deposit is in the Tongren-Xiahe-Hezuo polymetallic district in the westernmost West Qinling orogenic belt. The estimated pre-mining resource is approximately 13.6 t of Au at an average grade of 3.02 g/t. Mineralization is predominantly controlled by NW-trending and EW-trending faults within diorite intrusions and surrounding sedimentary rocks. In the present study, in situ zircon U–Pb geochronology and Lu–Hf isotopic analyses of the ore-hosting diorite at Zaorendao were measured using LA-ICP-MS. The data suggest that the diorite was emplaced at ca. 246.5 ± 1.9 Ma. The large variation of zircon Hf isotopic composition ($\epsilon_{\text{Hf}}(t)$) values ranging from -12.0 to -1.8 indicates a two-stage model age ($T_{\text{DM}2}$) that ranges from 1.4 Ga to 2.0 Ga. Such Lu–Hf isotopic compositions indicate that the diorite was dominantly derived from a Paleo- to Meso-Proterozoic continental crust. The wide range of $\epsilon_{\text{Hf}}(t)$ and the presence of inherited zircon can be interpreted to suggest the mixing of Paleo- to Meso-Proterozoic continental crust with a mantle component. Combining such characteristics with the geochemistry of coeval rocks that are associated with the diorite, we therefore proposed that the gold-hosting Triassic diorite in the Zaorendao gold deposit formed in an active continental margin that was associated with the northward subduction of the paleo-Tethyan ocean.

Keywords: geochronology; Hf isotopes; petrogenesis; paleo-Tethyan ocean closure; Zaorendao gold deposit; West Qinling

1. Introduction

The WNW-trending West Qinling orogen, the western half of the Qinling orogen, is connected to the Kunlun Orogen and the Qaidam terrane in the west [1,2]. The West Qinling orogen evolved over a protracted period from the Proterozoic up to the late Mesozoic. The tectonic history evolved in response to subduction and closure of the paleo-Tethys ocean and subsequent continental collision between the South China block and North China block during Late Triassic (Figure 1) [1–6]. This region contains abundant Cu–Au, Cu–Mo, Au, Au–Sb, and Pb–Zn deposits, and is known to be one of the most

important polymetallic belts in China [3,7–14]. Most of the gold deposits are hosted in Cambrian to Early Triassic marine sedimentary rocks and these deposits have been suggested to be either orogenic [3,15,16] or Carlin-like [9,17]. Widespread magmatic activity in the West Qinling orogen is temporally and/or spatially associated with several types of gold mineralization, which include porphyry Cu-Au deposits, skarn-type Cu-Au (-Fe) deposits, and lode/disseminated Au deposits [12,18–20]. Thus, information on the widespread Triassic granitoids closely associated with the deposits in the West Qinling is important to constrain the tectono-magmatic and mineralization processes.

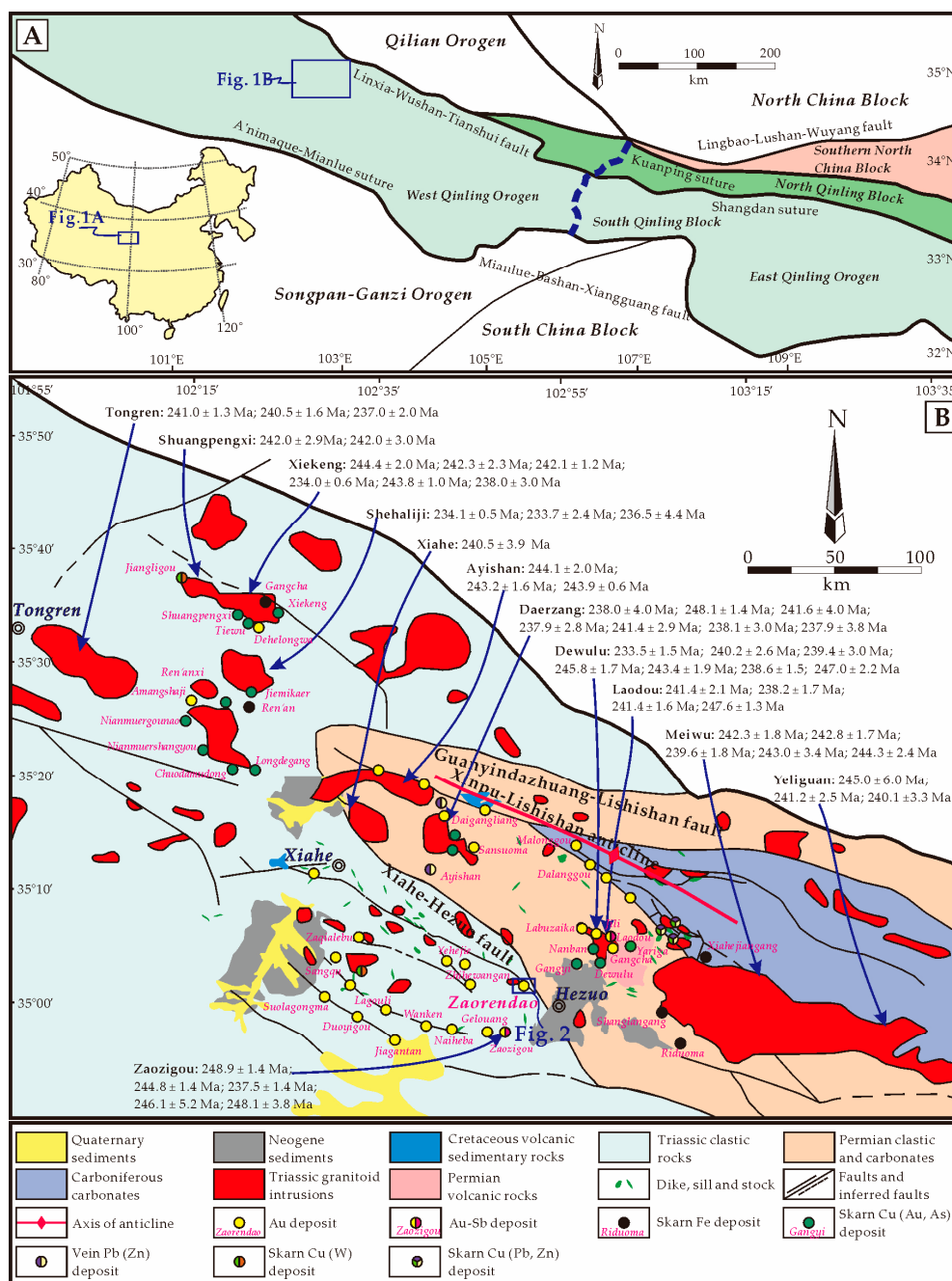


Figure 1. (A) Major tectonic domains of China and the location of the Qinling Orogenic Belt. Inset shows the location of the study area (modified after [12]). (B) Simplified geological map of the Tongren-Xiahe-Hezuo district of the West Qinling orogen, showing distributions and ages of Early Triassic granitoids and ore deposits (modified after [12] and [21]).

The Tongren-Xiahe-Hezuo district, located to the northwestern section of the West Qinling, contains numerous sediment- and/or dike-hosted disseminated and lode gold deposits, as well as many Cu-Au-W-Fe skarn deposits, and has been one of the most popular districts for exploring metal resources over the last decade (Figure 1) [12,19,22]. The relationship between the disseminated gold deposits to the south of Xiahe-Hezuo fault and magmatism is controversial and poorly understood, due to the rare constraints on the emplacement age and petrogenesis of stocks and dikes.

The newly discovered Zaorendao gold deposit is one of largest in the Tongren-Xiahe-Hezuo polymetallic district. The diorite stock and surrounding sedimentary rocks that are cut by NW-trending and nearly EW-trending fracture belts host the dominant gold mineralization. However, no petrography, geochronology, or geochemistry research on the diorite has been conducted until now. Based on systematic field investigations and petrographic observations, we present zircon LA-ICP-MS U–Pb geochronology, and Lu–Hf isotopic composition of the ore-hosting diorite in the Zaorendao deposit, to: a) establish the time of its emplacement, b) understand the petrogenesis of the diorite.

2. Geological Background

2.1. Regional Geology

The E-W-trending Qinling orogen in central China, which extends for more than 1500 km and is ~200–250 km wide, is tectonically situated between the North China and the South China blocks (Figure 1A) [1,23]. The Lingbao-Lushan-Wuyang fault separates the West Qinling orogen from the Qilian Orogen and North China block to the north. The West Qinling orogen is separated from the Songpan-Ganzi Orogen and the South China block in the south by the Mianlue-Bashan-Xiangguang fault [2,23,24]. The Qinling orogen is further divided into Southern North China block, North Qinling and South Qinling blocks by the Kuanping and Shangdan sutures [1,25–27].

The West Qinling orogen, the western part of the Qinling orogen, is traditionally separated from the East Qinling orogen by the Huicheng basin or Foping dome, which can be observed as roughly marked by the Baoji-Chengdu railway line (shown as blue dash line in Figure 1A) [25,28]. The West Qinling orogen is bounded by the Linxia-Wushan-Tianshui fault (Shangdan suture) on the north and the A'nimaque–Mianlue suture on the south (Figure 1A) [24,29,30]. The West Qinling had a protracted and complex evolution history from the Proterozoic up to the late Mesozoic, with the final collision between the South China block and the South Qinling block along the A'nimaque–Mianlue suture zone [1,3,23,30–32]. The West Qinling orogen is dominantly covered by Paleozoic to early Mesozoic marine sedimentary rocks that were deformed in the early Mesozoic [2,33], and intruded by numerous Mesozoic granitoid intrusions. The widespread Mesozoic igneous rocks are grouped into subduction-related granitoids with ages ranging from ca. 250–235 Ma, syn-collision granitoids with ages ranging from ca. 228–215 Ma and post-collisional granitoids with ages ranging from ca. 210–190 Ma [4,11,13,34–36]. This is interpreted to be due to the northward subduction of paleo-Tethys ocean and subsequent syn-collision to post-collision between the North China and South China blocks.

The Tongren-Xiahe-Hezuo district is located to the northwestern section of West Qinling (Figure 1B) [12,19,21,37]. The exposed strata are dominated by weakly metamorphosed to un-metamorphosed marine sedimentary rocks of Carboniferous to Triassic age (Figure 1B) [12,19,21,37]. The Carboniferous rocks consist mainly of sandstone, siltstones, thin- to thick-bedded limestones and clastic limestone, whereas the Permian slope to deep-marine basinal facies rocks are mainly composed of carbonaceous/argillaceous siltstone, sandstone, conglomerate, limestone and calcirudite. The Lower to Middle Triassic strata comprise interbedded sandstones, siltstones, calcareous siltstones, and mudstones, with minor amounts of siliceous nodules hosted by siltstone layers [12,19,21]. The Carboniferous carbonates and siltstones, and Permian marine clastic and carbonates are exposed mainly in the core and both flanks of the Xinpu-Lishishan anticline, respectively, and cover the central to southeast part of the district. The Triassic strata are separated from Carboniferous and Permian rocks by the Guanyindazhuang-Lishishan fault to the north and Xiahe-Hezuo fault to the south [12],

and are exposed in the west of the district. Several dioritic to granitic plutons, represented by the Tongren, Jiangligou, Shuangpengxi, Xiekeng, Shehaliji, Xiahe, Ayishan, Daerzang, Dewulu, Laodou, Meiwu and Yeliguan plutons/batholiths, intrude the strata. These intrusions were emplaced between 250 and 234 Ma (Table 1) [12,37–41], and form a discontinuous NW-trending magmatic belt between the axial trace of the Xinpu-Lishishan anticline and the Xiahe-Hezuo fault. The magmatic belt extends northwest to the Tongren district [19,39]. Numerous stocks and dikes occur mainly to the south of the Xiahe-Hezuo fault, and these stocks and dikes are similar in composition to the plutons in the north. The emplacement age and petrogenesis of stocks and dikes is poorly constrained, but recent studies on zircon U–Pb age of dikes in the Zaozigou gold deposit indicate that they were emplaced in the 238–249 Ma interval, coeval with the plutons in the north [20,41]. A few tens of hydrothermal ore deposits and occurrences have been identified in the Tongren-Xiahe-Hezuo district, and these deposits are temporally and/or spatially associated with the Triassic granitoids (Figure 1B). Mineralization to the south of the Xiahe-Hezuo fault is mainly hosted by Triassic marine sedimentary rocks and, less significantly in the intermediate to felsic stocks and/or dikes. These deposits are characterized by disseminated gold deposits [42–44]. In the north part of the district, dozens of lode gold deposits and Cu–Au–(W)–(Fe) skarn deposits have been discovered hosted within or close proximity of intrusions [12,18,19].

Table 1. Compilation of previously published zircon U–Pb ages of the Triassic magmatism in the Tongren-Xiahe-Hezuo polymetallic district.

Pluton	Location	Rock	Age (Ma)	Method	Reference
Tongren	Tongren, Qinhai	Granodiorite	241.0 ± 1.3	LA-ICP-MS	Li et al., 2015 [37]
Tongren	Tongren, Qinhai	Granodiorite	240.5 ± 1.6	LA-ICP-MS	Li et al., 2015 [37]
Tongren	Tongren, Qinhai	Granodiorite	237.0 ± 2.0	LA-ICP-MS	Luo, 2013 [45]
Shuangpengxi	Tongren, Qinhai	Granodiorite	242.0 ± 2.9	LA-ICP-MS	Luo et al., 2012 [39]
Shuangpengxi	Tongren, Qinhai	Granodiorite	242.0 ± 3.0	SHRIMP	Zhang et al., 2014 [46]
Xiekeng	Tongren, Qinhai	Granodiorite	244.4 ± 2.0	LA-ICP-MS	Luo et al., 2012 [39]
Xiekeng	Tongren, Qinhai	Granodiorite	242.3 ± 2.3	LA-ICP-MS	Luo et al., 2012 [39]
Xiekeng	Tongren, Qinhai	Andesite	242.1 ± 1.2	LA-ICP-MS	Guo et al., 2012 [18]
Xiekeng	Tongren, Qinhai	Diorite	234.0 ± 0.6	LA-ICP-MS	Guo et al., 2012 [18]
Xiekeng	Tongren, Qinhai	Gabbro diorite	243.8 ± 1.0	LA-ICP-MS	Guo et al., 2012 [18]
Xiekeng	Tongren, Qinhai	Gabbro diorite	238.0 ± 3.0	SHRIMP	Zhang et al., 2014 [46]
Shehaliji	Tongren, Qinhai	Quartz monzonite	234.1 ± 0.5	LA-ICP-MS	Huang et al., 2014 [47]
Shehaliji	Tongren, Qinhai	Granodiorite porphyry	233.7 ± 2.4	LA-ICP-MS	Luo, 2013 [45]
Shehaliji	Tongren, Qinhai	Mafic enclave	236.5 ± 4.4	LA-ICP-MS	Luo, 2013 [45]
Ayishan	Xiahe, Gansu	Diorite	244.1 ± 2.0	LA-ICP-MS	Luo, 2013 [45]
Ayishan	Xiahe, Gansu	Granodiorite	243.2 ± 1.6	LA-ICP-MS	Luo, 2013 [45]
Ayishan	Xiahe, Gansu	Granodiorite	243.9 ± 0.6	LA-ICP-MS	Wei, 2013 [48]
Xiahe	Xiahe, Gansu	Granodiorite	240.5 ± 3.9	LA-ICP-MS	Luo, 2013 [45]
Daerzang	Xiahe, Gansu	Quartz diorite porphyry	238.0 ± 4.0	SHRIMP	Jin et al., 2005 [38]
Daerzang	Xiahe, Gansu	Granodiorite	248.1 ± 1.4	LA-ICP-MS	Wei, 2013 [48]
Daerzang	Xiahe, Gansu	Granodiorite	241.6 ± 4.0	LA-ICP-MS	Xu et al., 2014 [40]
Daerzang	Xiahe, Gansu	Granodiorite	237.9 ± 2.8	LA-ICP-MS	Luo, 2013 [45]
Daerzang	Xiahe, Gansu	Quartz diorite	241.4 ± 2.9	LA-ICP-MS	Luo, 2013 [45]
Daerzang	Xiahe, Gansu	Biotite granite	238.1 ± 3.0	LA-ICP-MS	Luo, 2013 [45]
Daerzang	Xiahe, Gansu	Mafic enclave	237.9 ± 3.8	LA-ICP-MS	Luo, 2013 [45]
Dewulu	Hezuo, Gansu	Granodiorite	233.5 ± 1.5	LA-ICP-MS	Xu et al., 2014 [40]
Dewulu	Hezuo, Gansu	Granodiorite	240.2 ± 2.6	LA-ICP-MS	Luo, 2013 [45]
Dewulu	Hezuo, Gansu	Granodiorite	239.4 ± 3.0	LA-ICP-MS	Luo, 2013 [45]
Dewulu	Hezuo, Gansu	Quartz diorite	245.8 ± 1.7	LA-ICP-MS	Zhang et al., 2015 [49]
Dewulu	Hezuo, Gansu	Quartz diorite	243.4 ± 1.9	LA-ICP-MS	Zhang et al., 2015 [49]
Dewulu	Hezuo, Gansu	Quartz diorite	238.6 ± 1.5	LA-ICP-MS	Jin et al., 2013 [50]
Dewulu	Hezuo, Gansu	Dioritic Mafic enclave	247.0 ± 2.2	LA-ICP-MS	Qiu and Deng, 2017 [12]
Laodou	Hezuo, Gansu	Granodiorite	241.4 ± 2.1	LA-ICP-MS	Zhang et al., 2015 [49]
Laodou	Hezuo, Gansu	Granodiorite	238.2 ± 1.7	LA-ICP-MS	Zhang et al., 2015 [49]
Laodou	Hezuo, Gansu	Granodiorite	241.4 ± 1.6	LA-ICP-MS	Zhang et al., 2015 [49]
Laodou	Hezuo, Gansu	Quartz diorite porphyry	247.6 ± 1.3	LA-ICP-MS	Jin et al., 2013 [50]
Yeliguan	Hezuo, Gansu	Quartz diorite	245.0 ± 6.0	SHRIMP	Jin et al., 2005 [38]
Yeliguan	Hezuo, Gansu	Quartz diorite	241.2 ± 2.5	LA-ICP-MS	Luo, 2013 [45]
Yeliguan	Hezuo, Gansu	Quartz diorite	240.1 ± 3.3	LA-ICP-MS	Luo, 2013 [45]
Meiwu	Hezuo, Gansu	Granodiorite	242.3 ± 1.8	LA-ICP-MS	Luo, 2013 [45]
Meiwu	Hezuo, Gansu	Granodiorite	242.8 ± 1.7	LA-ICP-MS	Luo, 2013 [45]
Meiwu	Hezuo, Gansu	Mafic enclave	239.6 ± 1.8	LA-ICP-MS	Luo, 2013 [45]
Meiwu	Hezuo, Gansu	Mafic enclave	243.0 ± 3.4	LA-ICP-MS	Luo, 2013 [45]
Meiwu	Hezuo, Gansu	Biotite granite	244.3 ± 2.4	LA-ICP-MS	Luo, 2013 [45]
Zaozigou	Hezuo, Gansu	Granodiorite	248.9 ± 1.4	LA-ICP-MS	Sui et al., 2018 [20]
Zaozigou	Hezuo, Gansu	Quartz diorite porphyry	244.8 ± 1.4	LA-ICP-MS	Sui et al., 2018 [20]
Zaozigou	Hezuo, Gansu	Diorite porphyry	237.5 ± 1.4	LA-ICP-MS	Sui et al., 2018 [20]
Zaozigou	Hezuo, Gansu	Porphyritic dacite	246.1 ± 5.2	LA-ICP-MS	Yu et al., 2019 [41]
Zaozigou	Hezuo, Gansu	Porphyritic dacite	248.1 ± 3.8	LA-ICP-MS	Yu et al., 2019 [41]
Zaorendao	Hezuo, Gansu	Diorite	246.6 ± 1.9	LA-ICP-MS	This study

2.2. Geology of the Zaorendao Gold Deposit

The Zaorendao gold deposit (102°50'59"E, 35°01'57"N, also referred to as Jiademu deposit), is located about 7 km northwestern of Hezuo in Gansu Province (Figure 1B). The estimated pre-mining resource of the Zaorendao deposit is approximately 13.6 t Au at an average grade of 3.02 g/t [51].

The stratigraphic sequence in the Zaorendao area is dominantly composed of slate, sandy slate and arkose of late Triassic age. The sedimentary sequence is up to 3047m in thickness and represents a shore to shallow sea facies. These sedimentary rocks are intruded by two diorite stocks and numerous intermediate to felsic dikes (Figure 2). The dioritic stocks, named the West rock and the East rock, are exposed in the central and northwestern part of the mining area. The East rock outcrops have a rectangle-shape with approximately area of 0.19 km², while the square-shaped West rock has an exposed area of 0.12 km². Another barren, small diorite stock is also exposed to the northeast of the East rock. The dikes mainly consist of porphyritic diorite, porphyritic granodiorite, and porphyritic quartz diorite. These dikes are 20~250 m long, 0.3~16 m wide, and cut across bedding of the Early Triassic slate.

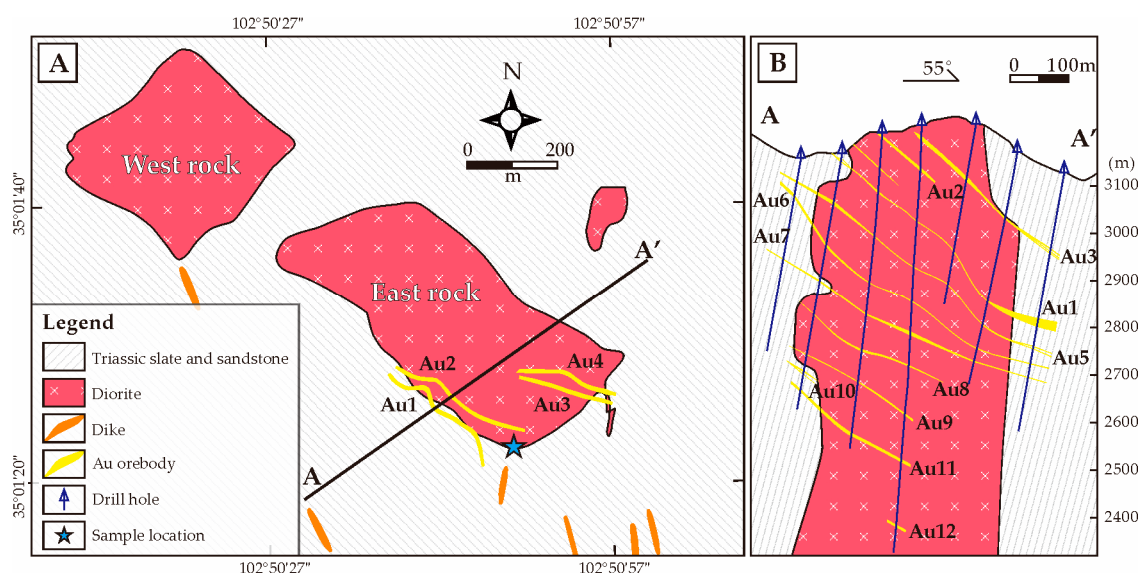


Figure 2. (A) Sketch geologic map of the Zaorendao gold deposit and (B) selected exploration cross section showing the occurrence of gold ores (after [51]).

One hundred and ninety-nine orebodies have been delineated in the Zaorendao mine, among which are six major orebodies, including Au1, Au2, Au5, Au6, Au7 and Au8 orebodies. These orebodies contain approximately 85% of the total gold reserves. Mineralization is controlled predominantly by the NW-trending faults cutting through the diorite and surrounding sedimentary rocks. These orebodies, striking NW 310° to 330° and dipping NE, and are a few meters thick and hundreds of meters long. The downward extent of the orebodies dip from 3227 m to 2366 m above sea level.

Hydrothermal alteration mineral assemblages in the mining area includes hydrothermal pyrite, arsenopyrite, stibnite, sericite, silicification, hematite and carbonate. Ore minerals are dominated by pyrite, arsenopyrite, and stibnite, with lesser sphalerite, chalcocite, galena, and hematite. The gangue minerals include sericite, quartz, epidote, biotite, plagioclase and calcite (Figure 3).

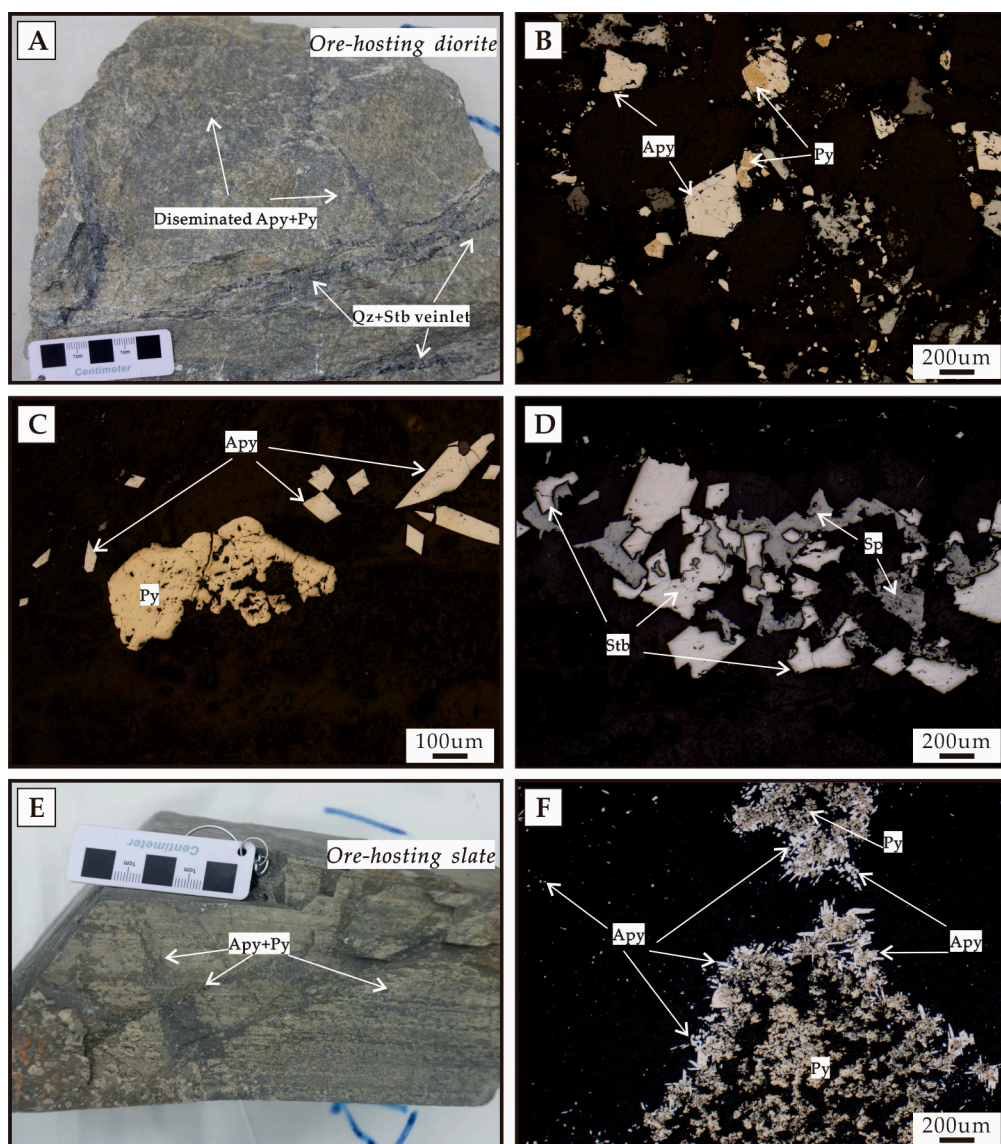


Figure 3. Photographs (A,E) and photomicrographs under reflected light (B–D,F) showing mineralization styles and mineral assemblages. Disseminations of pyrite and arsenopyrite in diorite (A–C). Stibnite veinlet in diorite (A,D). Disseminations of pyrite and arsenopyrite in slate (E,F). Mineral abbreviations: Apy = arsenopyrite, Py = pyrite, Qz = quartz, Sp = sphalerite, Stb = stibnite.

3. Sampling Strategy and Analytical Procedures

3.1. Sampling Strategy

One representative, minimally altered and relatively pristine sample of diorite (17ZRD01) was collected from surface on the Zaorendao gold mine premises (Figure 4A,B). This samples were used for zircon separation and laser ablation-inductively coupled plasma-mass spectrometry (LA-ICP-MS) U–Pb dating and Lu–Hf isotope analyses. The sampling locations are shown in Figure 2. The grey to sage-green diorite has medium-grained texture, and is mainly composed of plagioclase (~65 vol. %, 0.5–1.5 mm), biotite (~20 vol. %), and quartz (5–10 vol. %) with minor hornblende and pyroxene (Figure 4C,D). Accessory minerals are titanite, apatite and zircon. Plagioclase shows polysynthetic twinning and oscillatory zoning, and is locally altered to sericite (Figure 4C).

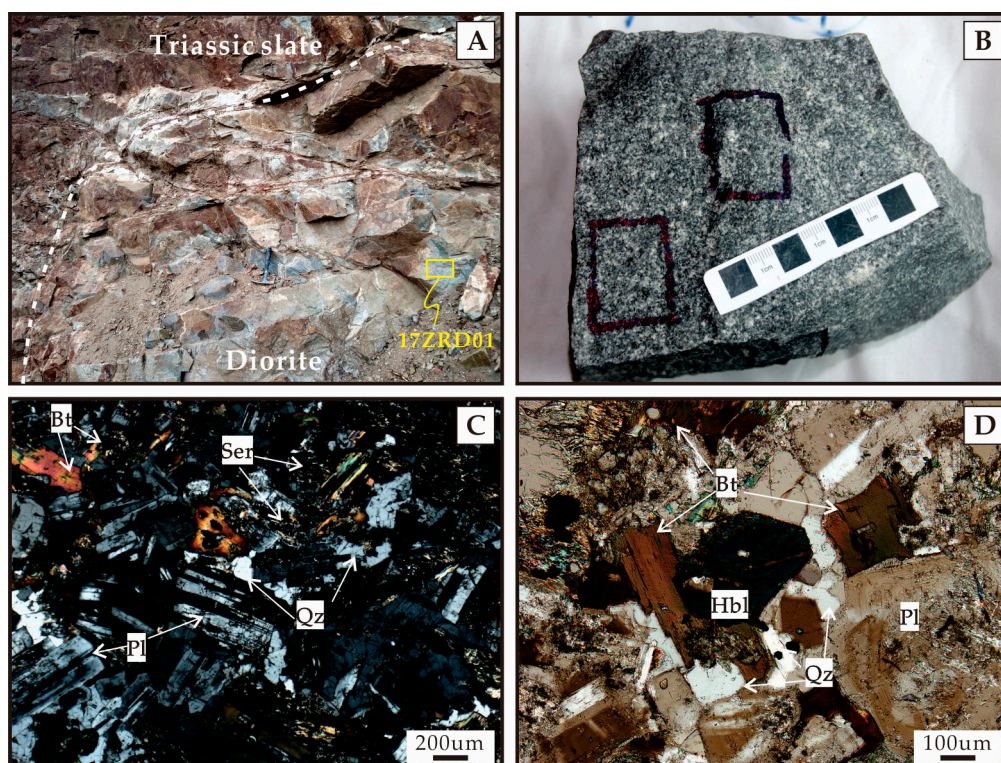


Figure 4. Photographs and photomicrographs of the diorite in the Zaorendao deposit showing its geologic relationship with Triassic slate (A) and texture and mineral association (B–D). Blue box lines in Figure (B) show locations of doubly polished thin sections. Mineral abbreviations: Bt = biotite, Hbl = hornblende, Pl = plagioclase, Qz = quartz, Ser = sericite.

3.2. Analytical Procedures

3.2.1. Zircon LA-ICP-MS U–Pb Dating and Trace-Element Analyses

Zircon crystals were separated from crushed diorite sample through standard magnetic and density separation techniques. The crystals were then carefully handpicked under a binocular microscope, mounted in epoxy, and polished down to approximately half sections to expose internal structures. To identify the internal structure and texture of the zircon grains and to select potential locations for U–Pb analysis, the mount was photographed in transmitted and reflected light, and cathodoluminescence (CL). The CL images were taken on a JXA-880 electron microscope (JEOL Ltd., Akishima, Tokyo, Japan) and an image analysis software was used under operating conditions of 20 kV and 20 nA at the Institute of Mineral Resources, Chinese Academy of Geological Sciences, Beijing, China.

Zircons were analyzed in situ for U, Th, and Pb isotope composition by a LA-ICP-MS system at the Isotopic Laboratory, Tianjin Institute of Geology and Mineral Resources of China Geological Survey, using a Neptune multiple-collector inductively coupled plasma-mass spectrometer (Thermo Fisher Ltd., Waltham, MA, USA) to a NEW WAVE 193 nm-FX ArF Excimer laser-ablation system (Elemental Scientific, Inc., Omaha, NE, USA). The analytical procedures are described in Reference [4]. The analyses were carried out with a pulse rate of 8 Hz, beam energy of 11 J/cm², and a spot diameter of 30 μm. Helium was used as a carrier gas. The NIST SRM 610 glass standard was used as an external standard to normalize U, Th, and Pb concentrations of the unknowns. Plešovice zircon, a new natural reference material for U–Pb isotopic microanalysis, and 91500 zircon were used as internal standards for U–Pb dating, and were both analyzed twice every 8 unknown zircons analyses, to normalize isotopic fractionation during isotope analysis. Common-Pb corrections were made using the method of Anderson [52]. ²⁰⁷Pb/²⁰⁶Pb, ²⁰⁶Pb/²³⁸U, ²⁰⁷Pb/²³⁵U and ²⁰⁸Pb/²³²Th ratios were calculated from

measured ion intensities using ICPMSDataCal 8.4 [53]. Concordia diagrams and weighted mean U–Pb ages were processed using ISOPLOT 3 [54]. Age data and concordia plots were reported at 1σ error, whereas the uncertainties for weighted mean ages are given at 95% confidence level.

3.2.2. In situ Zircon Lu–Hf Isotope Analyses

The same domains or the same zircon zones that had been analyzed for U–Pb were analyzed for their Lu–Hf isotopic composition at the Isotopic Laboratory, Tianjin Institute of Geology and Mineral Resources of China Geological Survey, following the method described in Reference [4] and using a Thermo Finnigan Neptune MC-ICP-MS system coupled to a New Wave UP193 nm laser-ablation system. The analyses were carried out with a laser repetition rate of 11 Hz at 100 mJ, and a spot diameter of 50 μm . Helium was used as a carrier gas. During the analyses, the zircon GJ-1 was analyzed as quality control every 8 unknown samples, and yielded $^{176}\text{Hf}/^{177}\text{Hf}$ ratios of 0.282023 ± 30 (2σ , $n = 12$). Results excellently coincide with the recommended $^{176}\text{Hf}/^{177}\text{Hf}$ ratios of 0.282015 ± 19 [55] for GJ-1.

For calculation of initial epsilon Hf ($\epsilon_{\text{Hf}}(t)$) values, the decay constant of 1.865×10^{-11} [56] and the values for the chondritic uniform reservoir (CHUR, $^{176}\text{Lu}/^{177}\text{Hf} = 0.0332$, $^{176}\text{Hf}/^{177}\text{Hf} = 0.282772$ [57]) were used. The initial $^{176}\text{Hf}/^{177}\text{Hf}$ ratios and $\epsilon_{\text{Hf}}(t)$ for all analyzed zircon domains were calculated by the corresponding $^{206}\text{Pb}/^{238}\text{U}$ age. The single stage depleted mantle model ages (T_{DM}) were determined for each sample by calculating the intersection of the zircon/parent-rock growth trajectory with the depleted mantle evolution curve [58] calculated with a present-day $^{176}\text{Hf}/^{177}\text{Hf}$ ratio of 0.28235 (similar to mid-ocean ridge basalts values [59] and $^{176}\text{Lu}/^{177}\text{Hf}$ of 0.0384 [60] for the depleted mantle (DM). The two stages DM Hf model age ($T_{\text{DM}2}$) was calculated for the source rock of the magma from the initial $^{176}\text{Hf}/^{177}\text{Hf}$ of each zircon at the time of crystallization (in terms of the apparent $^{206}\text{Pb}/^{238}\text{U}$ age) by using $^{176}\text{Lu}/^{177}\text{Hf} = 0.015$ for the average crust [61].

4. Analytical Results

4.1. Zircon U–Pb Morphology and Geochronology

Cathodoluminescence images of representative analyzed zircons for U–Pb and Lu–Hf analyses are illustrated in Figure 5. The LA-ICP-MS zircon U–Pb analytical data for diorite sample 17ZRD01 are presented in Table 2 and graphically illustrated in the concordia diagrams (Figure 6).

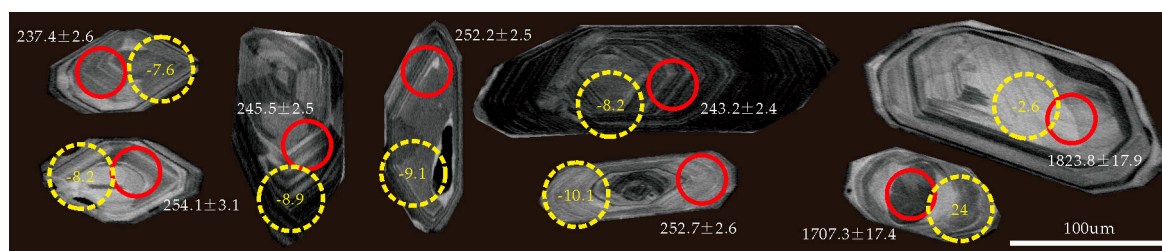


Figure 5. Representative CL images of zircons separated from diorite sample 17ZRD01 with identified analytical spot, U–Pb age (Ma) and $\epsilon_{\text{Hf}}(t)$ value. Red circle: U–Pb beam. Yellow dash circle: Lu–Hf beam.

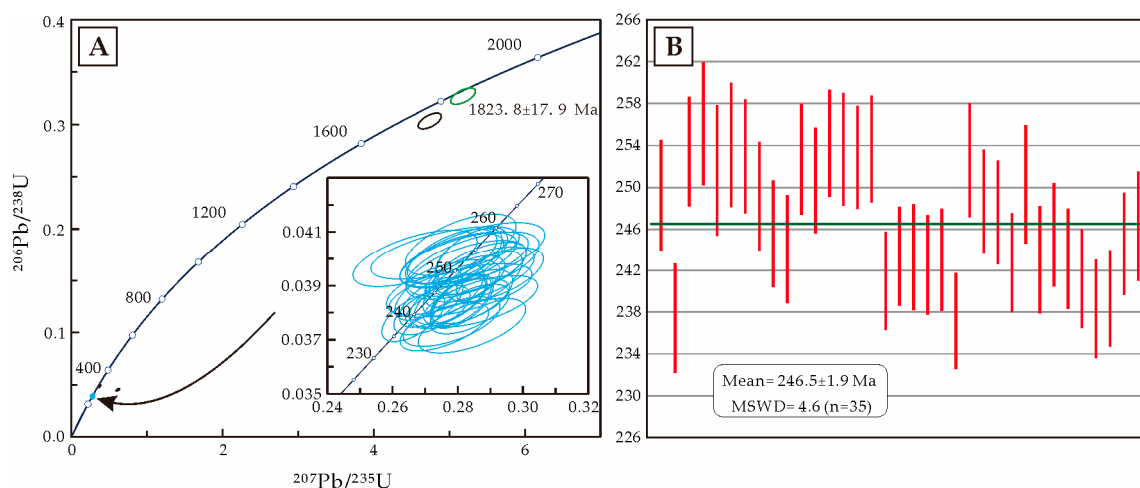


Figure 6. Zircon LA-ICP-MS U–Pb concordia diagrams for the ore-hosting diorite sample 17ZRD01.

Zircons separated from sample 17ZRD01 are mostly colorless to pale yellow, transparent, and commonly euhedral prismatic to elongated prismatic. The length of zircons varies from 90 to 250 μm with aspect ratios of 5:1 to 2:1. Most zircon grains show oscillatory zoning in CL images (Figure 5), consistent to that of igneous zircons [62]. Some grains display a core-rim structure consisting of an inherited core with distinct oscillatory and patchy zoning (Figure 5).

Thirty-nine analyses were carried out for U–Pb dating on sample 17ZRD01, yielding U–Pb ages ranging from 237.2 ± 2.3 Ma to 1823.8 ± 17.9 Ma. Thirty-seven analyses were obtained from the zircons with oscillatory zoning, among which, two analyses (spot 17ZRD01.10, 17ZRD01.17) give $^{206}\text{Pb}/^{238}\text{U}$ dates of 285.0 ± 3.0 Ma and 306.4 ± 3.2 Ma, and are excluded because they are statistical outliers. The remaining 35 analyses are concordant, with $^{206}\text{Pb}/^{238}\text{U}$ dates ranging from 237.2 ± 2.3 Ma to 256.1 ± 2.9 Ma with a weighted mean of 246.5 ± 1.9 (MSWD = 4.6, Figure 6). The Th/U ratios of the zircons are between 0.15 and 0.55, with an average of 0.34. The high Th/U values for the zircons suggest that they are magmatic in origin. The Th content ranges from 25.17 to 324.02 ppm, with an average of 104.43 ppm. The U content ranges from 97.60 to 1404.46 ppm, with an average of 344.91 ppm. The U–Pb age is therefore interpreted as the crystallization age of the diorite. One analysis (17ZRD01.27) on the zircon core yield $^{206}\text{Pb}/^{238}\text{U}$ age of 1707.3 ± 17.4 Ma is excluded because it is a statistical outlier. The remaining one analysis (spot 17ZRD01.36), gives a $^{206}\text{Pb}/^{238}\text{U}$ dates of 1823.8 ± 17.9 Ma with Th/U ratio of 0.17 (Table 2, Figures 5 and 6A). This is concordant and interpreted to be inherited during its emplacement.

4.2. Zircon Lu–Hf Isotopic Composition

In situ Hf isotope analyses have been carried out on zircons at the same spots used for zircon U–Pb dating. Zircon Lu–Hf isotopic data are presented in Table 3, and shown in Figure 7. The Hf isotopic data, expressed as values of epsilon Hf ($\epsilon_{\text{Hf}}(t)$) at the time of emplacement, from the 17ZRD01 are plotted versus time in Figure 7.

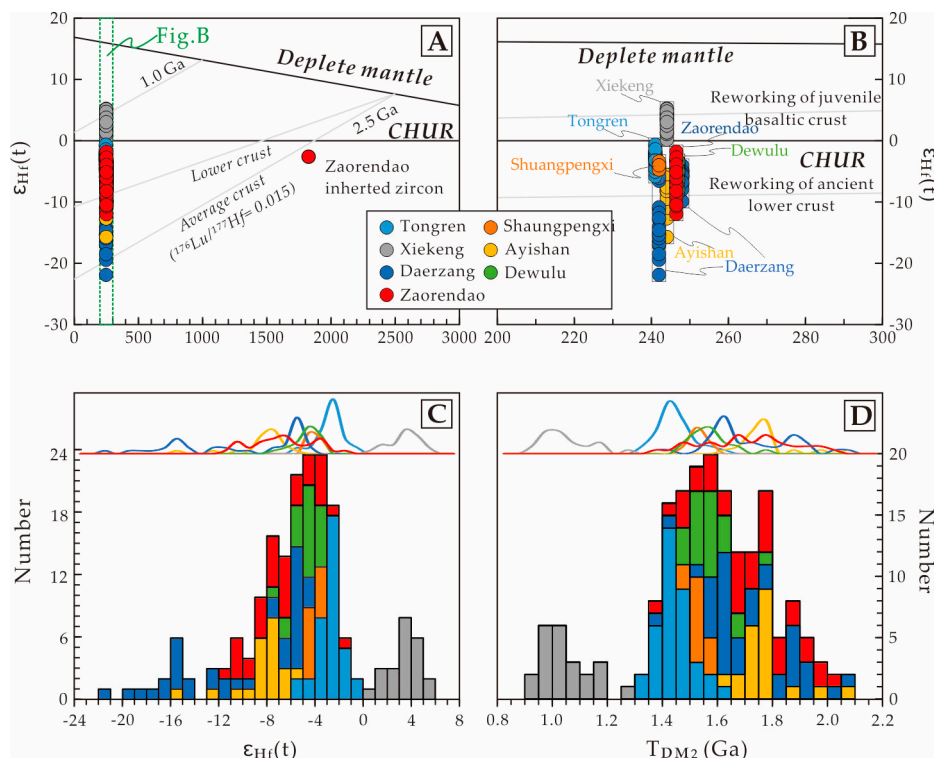


Figure 7. Plots of $\epsilon_{Hf}(t)$ values vs. U-Pb ages for zircons from the diorite in the Zaorendao deposit (A, B). (C) Histogram, and frequency curves of $\epsilon_{Hf}(t)$ values. (D) Histogram, and frequency curves of corresponding two-stage model age (T_{DM2}). Date from the igneous rocks of Tongren-Xiahe-Hezuo district are shown (Date are from Reference [12] and references therein).

The 35 analyses for an estimated age at ca. 247 Ma yield $^{176}\text{Lu}/^{177}\text{Hf}$ and $^{176}\text{Hf}/^{177}\text{Hf}$ ratios of 0.000093 to 0.001847 and 0.282278 to 0.282575. They display $\epsilon_{Hf}(t)$ values varying from -12.0 to -1.8 , with an average of -6.7 , and the two-stage model age (T_{DM2}) range from 1.4 Ga to 2.0 Ga with an average of 1.7 Ga. It may indicate the contributions of both juvenile and ancient crustal materials. The inherited core gives $^{176}\text{Lu}/^{177}\text{Hf}$ and $^{176}\text{Hf}/^{177}\text{Hf}$ ratios of 0.001655 and 0.281608, with $\epsilon_{Hf}(t)$ values of T_{DM2} of 2.6 Ga.

Table 2. Zircon LA-ICP-MS U–Pb data of the ore-hosting diorite in the Zaorendao deposit.

No. Spot	Element			Isotopic Ratios						Age (Ma)			
	Th (ppm)	U (ppm)	Th/U	²⁰⁷ Pb/ ²⁰⁶ Pb	1σ	²⁰⁷ Pb/ ²³⁵ U	1σ	²⁰⁶ Pb/ ²³⁸ U	1σ	²⁰⁷ Pb/ ²³⁵ U	1σ	²⁰⁶ Pb/ ²³⁸ U	1σ
17ZRD01.1	37.81	144.43	0.26	0.0528	0.0007	0.2867	0.0068	0.0394	0.0004	256.0	6.1	249.2	2.6
17ZRD01.2	43.84	160.35	0.27	0.0550	0.0013	0.2844	0.0067	0.0375	0.0004	254.1	6.0	237.4	2.6
17ZRD01.3	48.76	135.67	0.36	0.0503	0.0011	0.2783	0.0056	0.0401	0.0004	249.3	5.0	253.4	2.6
17ZRD01.4	41.56	155.62	0.27	0.0503	0.0008	0.2809	0.0069	0.0405	0.0005	251.4	6.2	256.1	2.9
17ZRD01.5	128.56	255.67	0.50	0.0519	0.0008	0.2846	0.0083	0.0398	0.0005	254.3	7.4	251.6	3.1
17ZRD01.6	36.38	110.39	0.33	0.0515	0.0008	0.2856	0.0086	0.0402	0.0005	255.1	7.7	254.1	3.0
17ZRD01.7	42.30	137.12	0.31	0.0484	0.0008	0.2669	0.0078	0.0400	0.0004	240.2	7.0	252.9	2.7
17ZRD01.8	72.33	160.50	0.45	0.0536	0.0009	0.2915	0.0060	0.0394	0.0004	259.7	5.4	249.1	2.6
17ZRD01.9	51.89	185.91	0.28	0.0525	0.0013	0.2809	0.0090	0.0388	0.0004	251.4	8.0	245.5	2.6
17ZRD01.10 *	443.87	1804.48	0.25	0.0983	0.0013	0.6127	0.0098	0.0452	0.0005	485.2	7.8	285.0	3.0
17ZRD01.11	147.61	312.24	0.47	0.0534	0.0007	0.2843	0.0051	0.0386	0.0004	254.0	4.6	244.1	2.6
17ZRD01.12	41.05	131.09	0.31	0.0508	0.0007	0.2802	0.0073	0.0400	0.0004	250.8	6.5	252.7	2.6
17ZRD01.13	324.02	1363.07	0.24	0.0525	0.0007	0.2868	0.0058	0.0396	0.0004	256.0	5.2	250.7	2.5
17ZRD01.14	40.50	155.23	0.26	0.0498	0.0009	0.2761	0.0093	0.0402	0.0004	247.6	8.4	254.2	2.5
17ZRD01.15	174.51	318.25	0.55	0.0514	0.0007	0.2842	0.0045	0.0401	0.0004	253.9	4.1	253.6	2.7
17ZRD01.16	79.95	152.98	0.52	0.0506	0.0013	0.2790	0.0062	0.0400	0.0004	249.9	5.5	252.9	2.5
17ZRD01.17 *	282.42	506.15	0.56	0.0555	0.0008	0.3723	0.0050	0.0487	0.0005	321.4	4.3	306.4	3.2
17ZRD01.18	164.32	385.89	0.43	0.0512	0.0007	0.2835	0.0041	0.0401	0.0004	253.4	3.7	253.7	2.6
17ZRD01.19	74.11	244.10	0.30	0.0518	0.0007	0.2721	0.0048	0.0381	0.0004	244.4	4.3	241.0	2.4
17ZRD01.20	126.05	304.49	0.41	0.0523	0.0007	0.2776	0.0045	0.0385	0.0004	248.8	4.0	243.4	2.4
17ZRD01.21	64.70	195.65	0.33	0.0522	0.0007	0.2771	0.0049	0.0385	0.0004	248.3	4.4	243.3	2.5
17ZRD01.22	38.30	144.45	0.27	0.0530	0.0008	0.2800	0.0065	0.0383	0.0004	250.6	5.8	242.6	2.4
17ZRD01.23	36.20	157.47	0.23	0.0542	0.0010	0.2870	0.0071	0.0384	0.0004	256.2	6.4	243.0	2.5
17ZRD01.24	77.77	191.50	0.41	0.0534	0.0022	0.2759	0.0056	0.0375	0.0004	247.4	5.0	237.2	2.3
17ZRD01.25	25.79	97.60	0.26	0.0512	0.0017	0.2820	0.0080	0.0400	0.0004	252.2	7.2	252.6	2.7
17ZRD01.26	307.45	1404.46	0.22	0.0534	0.0008	0.2896	0.0042	0.0393	0.0004	258.3	3.7	248.6	2.5
17ZRD01.27 *	125.41	340.95	0.37	0.1134	0.0015	4.7409	0.0627	0.3032	0.0031	1774.5	23.5	1707.3	17.4
17ZRD01.28	198.35	418.84	0.47	0.0523	0.0015	0.2821	0.0051	0.0392	0.0004	252.3	4.5	247.6	2.5
17ZRD01.29	149.27	784.68	0.19	0.0514	0.0008	0.2719	0.0040	0.0384	0.0004	244.2	3.6	242.8	2.4
17ZRD01.30	25.17	107.51	0.23	0.0518	0.0009	0.2827	0.0075	0.0396	0.0004	252.8	6.7	250.3	2.8
17ZRD01.31	185.97	498.31	0.37	0.0531	0.0008	0.2813	0.0040	0.0384	0.0004	251.7	3.5	243.0	2.6
17ZRD01.32	155.40	608.82	0.26	0.0521	0.0021	0.2787	0.0038	0.0388	0.0004	249.6	3.4	245.5	2.5
17ZRD01.33	199.16	1334.77	0.15	0.0531	0.0009	0.2813	0.0037	0.0384	0.0004	251.7	3.3	243.2	2.4
17ZRD01.34	138.04	272.51	0.51	0.0540	0.0011	0.2837	0.0049	0.0381	0.0004	253.6	4.4	241.2	2.4
17ZRD01.35	115.54	242.56	0.48	0.0536	0.0013	0.2781	0.0061	0.0377	0.0004	249.2	5.4	238.3	2.4
17ZRD01.36	44.76	257.28	0.17	0.1149	0.0020	5.1806	0.0673	0.3270	0.0032	1849.4	24.0	1823.8	17.9
17ZRD01.37	157.94	351.17	0.45	0.0511	0.0010	0.2664	0.0039	0.0378	0.0004	239.8	3.6	239.4	2.3
17ZRD01.38	54.58	318.64	0.17	0.0509	0.0010	0.2711	0.0042	0.0387	0.0004	243.6	3.8	244.6	2.5
17ZRD01.39	49.94	129.80	0.38	0.0513	0.0014	0.2756	0.0071	0.0389	0.0004	247.1	6.4	246.3	2.6

Note: Data marked with * are excluded while being calculated due to their discordance.

Table 3. Lu–Hf isotopic composition of zircons from the ore-hosting diorite in the Zaorendao deposit.

Sample No.	Age (Ma)	$^{176}\text{Yb}/^{177}\text{Hf}$	$^{176}\text{Lu}/^{177}\text{Hf}$	$^{176}\text{Hf}/^{177}\text{Hf}$	2σ	$(^{176}\text{Hf}/^{177}\text{Hf})_i$	$\epsilon_{\text{Hf}}(0)$	$\epsilon_{\text{Hf}}(t)$	$T_{\text{DM}}(\text{Ma})$	$T_{\text{DM2}}(\text{Ma})$	$f_{\text{Lu/Hf}}$
17ZRD01.1	249	0.028163	0.000842	0.282440	0.000044	0.282436	−11.7	−6.4	1144	1686	−0.97
17ZRD01.2	237	0.025482	0.000826	0.282413	0.000118	0.282409	−12.7	−7.6	1182	1754	−0.98
17ZRD01.3	253	0.036162	0.001121	0.282404	0.000045	0.282399	−13.0	−7.6	1203	1766	−0.97
17ZRD01.4	256	0.024469	0.000753	0.282394	0.000040	0.282390	−13.4	−7.9	1206	1784	−0.98
17ZRD01.5	252	0.031765	0.000994	0.282320	0.000052	0.282316	−16.0	−10.6	1317	1954	−0.97
17ZRD01.6	254	0.025813	0.000886	0.282386	0.000045	0.282382	−13.7	−8.2	1221	1804	−0.97
17ZRD01.7	253	0.011117	0.000376	0.282405	0.000040	0.282403	−13.0	−7.5	1179	1757	−0.99
17ZRD01.8	249	0.032364	0.000968	0.282443	0.000042	0.282439	−11.6	−6.3	1144	1680	−0.97
17ZRD01.9	246	0.027803	0.000895	0.282440	0.000047	0.282436	−11.7	−6.5	1145	1687	−0.97
17ZRD01.10 *	285	0.042466	0.001449	0.282504	0.000045	0.282496	−9.5	−3.5	1072	1528	−0.96
17ZRD01.11	244	0.019020	0.000679	0.282429	0.000046	0.282426	−12.1	−6.9	1154	1711	−0.98
17ZRD01.12	253	0.017053	0.000537	0.282332	0.000047	0.282329	−15.6	−10.1	1285	1923	−0.98
17ZRD01.13	251	0.040060	0.001254	0.282533	0.000045	0.282527	−8.4	−3.2	1025	1479	−0.96
17ZRD01.14	254	0.033660	0.001277	0.282363	0.000041	0.282357	−14.5	−9.1	1267	1860	−0.96
17ZRD01.15	254	0.027274	0.000823	0.282423	0.000047	0.282419	−12.3	−6.9	1167	1721	−0.98
17ZRD01.16	253	0.013977	0.000388	0.282278	0.000052	0.282276	−17.5	−12.0	1354	2042	−0.99
17ZRD01.17 *	306	0.059984	0.002180	0.282262	0.000046	0.282250	−18.0	−11.8	1443	2065	−0.93
17ZRD01.18	254	0.032326	0.001056	0.282524	0.000043	0.282519	−8.8	−3.4	1033	1497	−0.97
17ZRD01.19	241	0.020187	0.000663	0.282418	0.000041	0.282415	−12.5	−7.3	1169	1737	−0.98
17ZRD01.20	243	0.038346	0.001120	0.282536	0.000045	0.282531	−8.3	−3.2	1017	1476	−0.97
17ZRD01.21	243	0.020875	0.000660	0.282499	0.000044	0.282496	−9.7	−4.4	1057	1556	−0.98
17ZRD01.22	243	0.025903	0.000942	0.282485	0.000035	0.282481	−10.1	−5.0	1084	1589	−0.97
17ZRD01.23	243	0.019343	0.000649	0.282456	0.000044	0.282453	−11.2	−5.9	1116	1651	−0.98
17ZRD01.24	237	0.023885	0.000747	0.282499	0.000049	0.282496	−9.7	−4.6	1059	1560	−0.98
17ZRD01.25	253	0.026457	0.000947	0.282381	0.000049	0.282377	−13.8	−8.4	1230	1816	−0.97
17ZRD01.26	249	0.024925	0.000797	0.282515	0.000050	0.282511	−9.1	−3.8	1039	1518	−0.98
17ZRD01.27 *	1707	0.010608	0.000320	0.282385	0.000046	0.282374	−13.7	24.0	1205	890	−0.99
17ZRD01.28	248	0.059339	0.001847	0.282363	0.000059	0.282354	−14.5	−9.3	1286	1870	−0.94
17ZRD01.29	243	0.021977	0.000730	0.282575	0.000038	0.282572	−7.0	−1.8	952	1385	−0.98
17ZRD01.30	250	0.026909	0.000810	0.282318	0.000040	0.282314	−16.1	−10.7	1313	1958	−0.98
17ZRD01.31	243	0.036243	0.001157	0.282474	0.000049	0.282469	−10.5	−5.4	1105	1616	−0.97
17ZRD01.32	245	0.004126	0.000112	0.282369	0.000047	0.282368	−14.3	−8.9	1220	1841	−1.00
17ZRD01.33	243	0.005910	0.000165	0.282390	0.000041	0.282390	−13.5	−8.2	1192	1794	−1.00
17ZRD01.34	241	0.039751	0.001183	0.282550	0.000045	0.282545	−7.8	−2.7	999	1446	−0.96
17ZRD01.35	238	0.038658	0.001139	0.282519	0.000048	0.282514	−9.0	−3.9	1042	1518	−0.97
17ZRD01.36	1824	0.056523	0.001655	0.281608	0.000051	0.281550	−41.2	−2.6	2345	2642	−0.95
17ZRD01.37	239	0.052997	0.001538	0.282334	0.000050	0.282327	−15.5	−10.5	1317	1936	−0.95
17ZRD01.38	245	0.003130	0.000093	0.282448	0.000047	0.282448	−11.5	−6.1	1111	1663	−1.00
17ZRD01.39	246	0.015306	0.000500	0.282477	0.000046	0.282475	−10.4	−5.1	1083	1601	−0.98

Note: Data marked with * are excluded while being calculated due to their discordance.

5. Discussion

5.1. Early to Middle Triassic Magmatism in Tongren-Xiahe-Hezuo Area

Zircon U–Pb dating of diorite in the Zaorendao suggests that the emplacement of diorite occurred at ca. 246.5 Ma, coeval with the widespread Triassic magmatism in the Tongren-Xiahe-Hezuo district (Table 1). Similar ages were obtained for the Tongren granodiorite (241 Ma [37]; 237 Ma [45]), Shuangpengxi granodiorite (242 Ma [39,46]), Xiekeng diorite–granodiorite (242–244 Ma [39]), Shehaliji quartz monzonite, Granodiorite porphyry and mafic microgranular enclaves (MME) (234 Ma [47]; 234–237 Ma [45]), Ayishan granodiorite (244 Ma [48]; 243–244 Ma [45]), Xiahe granodiorites (241 Ma [45]), Daerzang granodiorites (238 Ma [38]; 238–241 Ma [45]; 242 Ma [40]; 248 Ma [48]), Dewulu quartz diorite, quartz diorite porphyry and dioritic MME (238–247 Ma [12,49,50]), Laodou Granodiorite and Quartz diorite porphyry (238–241 Ma [49]; 248 Ma [50]), Meiwu granodiorite, biotite granite, and dioritic MME (240–244 Ma [45]), Yeliguan quartz diorite (240–241 Ma [45]; 245 Ma [38]). In addition, a recent study on the zircon U–Pb geochronology of granodiorite, quartz diorite porphyry diorite porphyry, and porphyritic dacites dikes in Zaozigou Au–Sb deposit to the northeast of the Zaorendao deposit indicate that the corresponding magmas were emplaced during 238–249 Ma [20,41]. We thus propose that the diorite of the Zaorendao deposit was emplaced during the Early Triassic, and was triggered by the same geodynamic processes as the widespread magmatism throughout the Tongren-Xiahe-Hezuo district.

5.2. Petrogenesis of Ore-Hosting Diorite

The diorite from the Zaorendao deposit yields relatively low $^{176}\text{Lu}/^{177}\text{Hf}$ and $^{176}\text{Hf}/^{177}\text{Hf}$ ratios (0.000093 to 0.001847 and 0.282278 to 0.282575), and has negative zircon $\epsilon_{\text{Hf}}(t)$ values varying from -12.0 to -1.8 with an average of -6.7 (Figure 7). The Lu–Hf isotopic composition is a sensitive tracer to detect the evolutionary history of the crust and mantle [58], by virtue of the fact that Hf partitions more strongly into the melt than Lu during mantle melting [63]. During the production of granitoid magmas, according to Belousova et al. [63], high values of $^{176}\text{Hf}/^{177}\text{Hf}$ ($\epsilon_{\text{Hf}} \gg 0$) indicate a ‘juvenile’ mantle input, either directly via mantle-derived mafic melts, or by remelting of a young mantle-derived mafic lower crust. The low values of $^{176}\text{Hf}/^{177}\text{Hf}$ (negative $\epsilon_{\text{Hf}}(t)$ values) provide evidence for crustal reworking. Mixing of crustal-derived and mantle-derived magmas during granite production can also be detected by inhomogeneity (including zoning) or wide variations in the Hf isotope composition and trace-element abundances in zircon populations [61,63]. The Hf isotopic composition therefore indicates that the source material of the diorite in the Zaorendao deposit is mainly the ancient crust-derived material.

Zircon Hf model ages represent a time when isotopic composition of zircon was the same as that of the parental magma that precipitated zircon. The two-stage Hf isotope model age (T_{DM2}), from which we assume that the sample was derived via melting of an average continental crust ($^{176}\text{Lu}/^{177}\text{Hf} = 0.015$) following derivation from the DM [63], range from 1.4 Ga to 2.0 Ga, with an average of 1.7 Ga. This indicates that the source material is mainly the Paleo- to Meso-Proterozoic crustal component. This is generally consistent with the analyses on the core (spot 17ZRD01.36) that yields a $^{206}\text{Pb}/^{238}\text{U}$ age of 1823.8 ± 17.9 Ma, and has been interpreted to be inherited. This indicates that this zircon grain could be inherited from a Paleoproterozoic basement during magma crystallization at ca. 246.5 Ma.

Another important feature of the Hf isotope data is the wide range of $\epsilon_{\text{Hf}}(t)$ values over 10 units. Such variations within a single sample can only be reconciled by the operation of open-system processes, such as magma mixing and/or assimilation [64–66]. The Hf isotope composition of the diorite from the Zaorendao deposit is very similar to the widespread coeval igneous rocks in the Tongren-Xiahe-Hezuo district (Figure 7). The Tongren granodiorite exhibits $\epsilon_{\text{Hf}}(t)$ values of -5.8 to -0.6 , with a corresponding T_{DM2} age of 1.31 to 1.64 Ga [37]. The Shuangpengxi granodiorite shows $\epsilon_{\text{Hf}}(t)$ values of -4.7 to -3.4 and T_{DM2} values of 1.49 to 1.57 Ga [39]. The Ayishan granodiorites have $\epsilon_{\text{Hf}}(t)$ values that range from -15.8 to -5.6 , with a corresponding T_{DM2} of 1.63 to 2.27 Ga [48].

The Da’erzang granodiorite exhibits $\epsilon_{\text{Hf}}(t)$ values ranging from -22.0 to -4.0 , with a corresponding T_{DM2} of 1.38 to 2.18 Ga [40,48]. The Dewulu granites have $\epsilon_{\text{Hf}}(t)$ values of -8.2 to -4.2 [67], while the dioritic MME have negative $\epsilon_{\text{Hf}}(t)$ values in the range of -8.0 to -3.3 with two-stage model ages that range from 1.48 to 1.78 Ga [12]. These granitoids turned out to be generated by melting of a lower crustal component with additional input of a mafic component derived from the mantle, indicating a regional magma mixing process [12]. Furthermore, the high Mg# values (58.25 and 60.00 [51]) of the diorite from the Zaorendao deposit are significantly higher than the melts produced by melting of metabasalts and eclogites (usually, $\text{Mg\#} < 45$ [68]), indicating that mixing of a basic magma is required for the origin. Thus, taking into account the regional occurrence of coeval igneous rocks (250–235 Ma), we propose that the Zaorendao diorite was derived mainly from the partial melting of ancient Paleo- to Meso-Proterozoic crustal material and has been mixed with a lesser number of mantle-derived components.

5.3. Geodynamic Implications

The widespread early to middle Triassic magmatism provide a window to better understand the geodynamic evolution of the Tongren-Xiahe-Hezuo polymetallic district. Li et al. [37] proposed that the Tongren granodiorite shows geochemical features of arc-related granitoids, and formed in a subduction-related regime in response to slab roll-back of the northward-subducting A’nimaque–Mianlue oceanic lithosphere. Combining zircon U–Pb dating with geochemical study of Shuangpengxi granodiorite pluton and the Xiekeng diorite–granodiorite pluton, Luo et al. [39] proposed that such magmatism resulted from break-off of the subducted oceanic slab after collision in the early stages of Indosinian orogeny. Guo et al. [18] argued that they are formed as a continental margin arc in northeastern Tibet due to northward subduction during consumption of the paleo-Tethys ocean. Huang et al. [47] reported zircon U–Pb ages of 234.1 Ma from the Shehaliji quartz monzonite, and suggested the Early Indosinian granitoids in the West Qinling were formed in an active continental margin. Wei [48] reported the Xiahe granitoids were emplaced between 244 to 248 Ma, and proposed that the Xiahe granitoids were formed in a continental margin arc setting. The Yeliguan quartz diorite and Xiahe quartz diorite porphyry show adakitic geochemical features, and have been interpreted to have formed in the active plate margin [38]. The petrology, geochronology and geochemistry of quartz diorite, quartz diorite porphyry and dioritic MME indicate that the granitoids in the Dewulu skarn copper deposit were products of arc magmatism in an active continental margin setting [12,50]. We therefore propose that the ore-hosting diorite from the Zaorendao deposit in this study and the coeval magmatism throughout the Tongren-Xiahe-Hezuo polymetallic district, formed along an active continental margin, and define a regionally similar geodynamic process associated with the northward subduction of the paleo-Tethyan ocean (Figure 8).

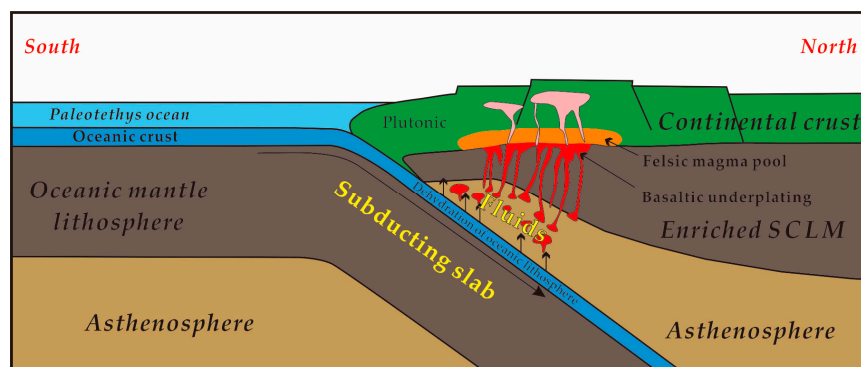


Figure 8. Schematic cartoon illustrating the petrogenesis of the ore-hosting diorite at Zaorendao and regional Triassic magmatism in the Tongren-Xiahe-Hezuo polymetallic district (modified after [12]). SCLM = sub-continental lithospheric mantle.

6. Conclusions

- (1) The gold-hosting diorite in the Zaorendao deposit yielded zircon LA-ICP-MS U-Pb age at 246.5 ± 1.9 Ma, coeval with the widespread Early Triassic magmatism in the Tongren-Xiahe-Hezuo district.
- (2) The ca. 247 Ma ore-hosting diorite is interpreted to have originated from the Paleo to Meso-Proterozoic continental crust, with lesser number of mantle-derived components.
- (3) The widespread Early Triassic magmatism in the Tongren-Xiahe-Hezuo polymetallic district probably formed along an active continental margin, corresponding to the northward subduction of the paleo-Tethyan ocean.

Author Contributions: Conceptualization, K.-F.Q.; Data curation, Z.-Y.G.; Investigation, Z.-Y.G., H.-C.Y., K.-F.Q. and Y.-G.W.; Methodology, J.-Z.G. and J.L.; Project administration, K.-F.Q.; Resources, Y.-G.W. and M.-H.Y.; Writing—original draft, Z.-Y.G. and K.-F.Q.; Writing—review and editing, H.-C.Y. and M.-Q.W.

Funding: This research was funded by the National Natural Science Foundation of China (41702069), China Postdoctoral Science Foundation (2016M591221, 20170108), CAS Key Laboratory of Mineral Resources (KLMR2017-03), State Key Laboratory of Geological Processes and Mineral Resources (MSFGPMR201804), and the Fundamental Research Funds for the Central Universities China (292018125, 292018141).

Acknowledgments: The authors thank Zhi-Lu Liang, Ding-Guo Jin, and Hong-Shun Ma from the Bureau of Geology and Mineral Exploration and Development of Gansu Province for their assistance in the field. Xue-Feng Li at the China University of Geosciences in Beijing is acknowledged for his assistance with petrography. The authors would also like to thank Duncan McIntire at Colorado School of Mines for assistance in editing this manuscript, and for scientific feedback.

Conflicts of Interest: The authors declare no conflict of interest.

References

1. Meng, Q.R.; Zhang, G.W. Geologic framework and tectonic evolution of the Qinling orogen, central China. *Tectonophysics* **2000**, *323*, 183–196. [[CrossRef](#)]
2. Dong, Y.P.; Zhang, G.W.; Neubauer, F.; Liu, X.M.; Genser, J.; Hauzenberger, C. Tectonic evolution of the Qinling orogen, China: Review and synthesis. *J. Asian Earth Sci.* **2011**, *41*, 213–237. [[CrossRef](#)]
3. Chen, Y.J.; Santosh, M. Triassic tectonics and mineral systems in the Qinling Orogen, China. *Geol. J.* **2014**, *49*, 338–358. [[CrossRef](#)]
4. Geng, J.Z.; Qiu, K.F.; Gou, Z.Y.; Yu, H.C. Tectonic regime switchover of Triassic Western Qinling Orogen: Constraints from LA-ICP-MS zircon U–Pb geochronology and Lu–Hf isotope of Dangchuan intrusive complex in Gansu, China. *Chem. Erde-Geochem.* **2017**, *77*, 637–651. [[CrossRef](#)]
5. Deng, J.; Wang, Q.F.; Li, G.J.; Santosh, M. Cenozoic tectono-magmatic and metallogenic processes in the Sanjiang region southwestern China. *Earth Sci. Rev.* **2014**, *138*, 268–299. [[CrossRef](#)]
6. Liu, Y.; Chakhmouradian, A.R.; Hou, Z.Q.; Song, W.L.; Kynický, J. Development of REE mineralization in the giant Maoniuping deposit (Sichuan, China): Insights from mineralogy, fluid inclusions, and trace-element geochemistry. *Miner. Deposita* **2018**. [[CrossRef](#)]
7. Deng, J.; Wang, Q.F.; Li, G.J. Tectonic evolution, superimposed orogeny, and composite metallogenic system in China. *Gondwana Res.* **2017**, *50*, 216–266. [[CrossRef](#)]
8. Liu, J.J.; Liu, C.H.; Carranza, E.J.M.; Li, Y.J.; Mao, Z.H.; Wang, J.P.; Wang, Y.H.; Zhang, J.; Zhai, D.G.; Zhang, H.F.; et al. Geological characteristics and ore-forming process of the gold deposits in the western Qinling region, China. *J. Asian Earth Sci.* **2014**, *103*, 40–69. [[CrossRef](#)]
9. Liu, J.J.; Dai, H.Z.; Zhai, D.G.; Wang, J.P.; Wang, Y.H.; Yang, L.B.; Mao, G.J.; Liu, X.H.; Liao, Y.F.; Yu, C.; et al. Geological and geochemical characteristics and formation mechanisms of the Zhaishang Carlin-like type gold deposit, western Qinling Mountains, China. *Ore Geol. Rev.* **2015**, *64*, 273–298. [[CrossRef](#)]
10. Deng, J.; Wang, Q.F. Gold mineralization in China: Metallogenic provinces, deposit types and tectonic framework. *Gondwana Res.* **2016**, *36*, 219–274. [[CrossRef](#)]
11. Qiu, K.F.; Taylor, R.D.; Song, Y.H.; Yu, H.C.; Song, K.R.; Li, N. Geologic and geochemical insights into the formation of the Taiyangshan porphyry copper-molybdenum deposit, Western Qinling Orogenic Belt, China. *Gondwana Res.* **2016**, *35*, 40–58. [[CrossRef](#)]

12. Qiu, K.F.; Deng, J. Petrogenesis of granitoids in the Dewulu skarn copper deposit: Implications for the evolution of the Paleotethys ocean and mineralization in Western Qinling, China. *Ore Geol. Rev.* **2017**, *90*, 1078–1098. [[CrossRef](#)]
13. Qiu, K.F.; Marsh, E.; Yu, H.C.; Pfaff, K.; Gulbransen, C.; Gou, Z.Y.; Li, N. Fluid and metal sources for the Wenquan porphyry molybdenite deposit, Western Qinling, NW China. *Ore Geol. Rev.* **2017**, *86*, 459–473. [[CrossRef](#)]
14. Deng, J.; Gong, Q.J.; Wang, C.M.; Carranza, E.J.M.; Santosh, M. Sequence of late Jurassic-early cretaceous magmatic-hydrothermal events in the Xiong'ershan region, central china: an overview with new zircon U-Pb geochronology data on quartz porphyries. *J. Asian Earth Sci.* **2014**, *79*, 161–172. [[CrossRef](#)]
15. Mao, J.W.; Qiu, Y.M.; Goldfarb, R.J.; Zhang, Z.C.; Garwin, S.; Ren, F.S. Geology, distribution, and classification of gold deposits in the western Qinling belt, central China. *Miner. Deposita* **2002**, *37*, 352–377. [[CrossRef](#)]
16. Yang, L.Q.; Deng, J.; Li, N.; Zhang, C.; Ji, X.Z.; Yu, J.Y. Isotopic characteristics of gold deposits in the yangshan gold belt, west Qinling, central china: Implications for fluid and metal sources and ore genesis. *J. Geochem. Explor.* **2016**, *168*, 103–118. [[CrossRef](#)]
17. Liu, D.S.; Tan, Y.J.; Wang, J.Y.; Wei, L.M. Carlin-type gold deposits in China. In *Chinese Carlin-Type Gold Deposits*; Liu, D.S., Tan, Y.J., Wang, J.Y., Eds.; Nanjing University Press: Nanjing, China, 1994; pp. 1–38. (In Chinese)
18. Guo, X.Q.; Yan, Z.; Wang, Z.; Wang, T.; Hou, K.; Fu, C.; Li, J. Middle Triassic arc magmatism along the northeastern margin of the Tibet: U–Pb and Lu–Hf zircon characterization of the Gangcha complex in the West Qinling terrane, Central China. *J. Geol. Soc.* **2012**, *169*, 327–336. [[CrossRef](#)]
19. Jin, X.Y.; Li, J.W.; Hofstra, A.H.; Sui, J.X. Magmatic-hydrothermal origin of the early Triassic Laodou lode gold deposit in the Xiahe-Hezuo district, West Qinling orogen, China: Implications for gold metallogeny. *Miner. Deposita* **2017**, *52*, 883–902. [[CrossRef](#)]
20. Sui, J.X.; Li, J.W.; Jin, X.Y.; Vasconcelos, P.; Zhu, R. $^{40}\text{Ar}/^{39}\text{Ar}$ and U–Pb constraints on the age of the Zaozigou disseminated gold deposit, Xiahe-Hezuo district, West Qinling orogen, China: Implications for the early Triassic reduced intrusion-related gold metallogeny. *Ore Geol. Rev.* **2018**, *101*, 885–899. [[CrossRef](#)]
21. Sui, J.X.; Li, J.W.; Wen, G.; Jin, X.Y. The Dewulu reduced Au–Cu skarn deposit in the Xiahe-Hezuo district, West Qinling orogen, China: Implications for an intrusion-related gold system. *Ore Geol. Rev.* **2017**, *80*, 1230–1244. [[CrossRef](#)]
22. Li, J.W.; Sui, J.X.; Jin, X.Y.; Wen, G.; Chang, J. A magmatic related gold system in the xiahe-hezuo district, western qinling orogen, china. *Acta Geol. Sin. Engl.* **2014**, *88*, 751–752. [[CrossRef](#)]
23. Yang, L.Q.; Ji, X.Z.; Santosh, M.; Li, N.; Zhang, Z.C.; Yu, J.Y. Detrital zircon U–Pb ages, Hf isotope, and geochemistry of Devonian chert from the Mianlue suture: Implications for tectonic evolution of the Qinling orogen. *J. Asian Earth Sci.* **2015**, *113*, 589–609. [[CrossRef](#)]
24. Ratschbacher, L.; Hacker, B.R.; Calvert, A.; Webb, L.E.; Grimmer, J.C.; McWilliams, M.O.; Ireland, T.; Dong, S.W.; Hu, J.M. Tectonics of the Qinling (central China): Tectonostratigraphy, geochronology, and deformation history. *Tectonophysics* **2003**, *366*, 1–53. [[CrossRef](#)]
25. Zhang, G.W.; Meng, Q.R.; Lai, S.C. Tectonics and structure of the Qinling Orogenic belt. *Sci. China Ser. B* **1995**, *38*, 1379–1394. (In Chinese)
26. Cao, H.H.; Li, S.Z.; Zhao, S.J.; Yu, S.; Li, X.Y.; Somerville, I.D. Detrital zircon geochronology of Neoproterozoic to early Paleozoic sedimentary rocks in the North Qinling Orogenic Belt: Implications for the tectonic evolution of the Kuanping Ocean. *Precambrian Res.* **2016**, *279*, 1–16. [[CrossRef](#)]
27. Li, S.Z.; Zhao, S.J.; Liu, X.; Cao, H.H.; Yu, S.; Li, X.Y.; Somerville, I.; Yu, S.Y.; Suo, Y.H. Closure of the Proto-Tethys Ocean and Early Paleozoic amalgamation of microcontinental blocks in East Asia. *Earth-Sci. Rev.* **2017**. [[CrossRef](#)]
28. Feng, Y.M.; Cao, X.D.; Zhang, E.P.; Hu, Y.X.; Pan, X.P.; Yang, J.L.; Jia, Q.Z.; Li, W.M. Tectonic evolution framework and nature of the west Qinling orogenic belt. *Northwest. Geol.* **2003**, *36*, 1–10, (In Chinese with English Abstract).
29. Deng, J.; Wang, Q.F.; Li, G.J.; Li, C.S.; Wang, C.M. Tethys tectonic evolution and its bearing on the distribution of important mineral deposits in the Sanjiang region, SW China. *Gondwana Res.* **2014**, *26*, 419–437. [[CrossRef](#)]
30. Dong, Y.P.; Yang, Z.; Liu, X.M.; Sun, S.S.; Li, W.; Cheng, B.; Zhang, F.F.; Zhang, X.N.; He, D.F.; Zhang, G.W. Mesozoic intracontinental orogeny in the Qinling Mountains, central China. *Gondwana Res.* **2016**, *30*, 144–158. [[CrossRef](#)]

31. Zhang, G.W.; Dong, Y.P.; Lai, S.C.; Guo, A.L.; Meng, Q.R.; Liu, S.F.; Cheng, S.Y.; Yao, A.P.; Zhang, Z.Q.; Pei, X.Z.; et al. Mianlue tectonic zone and Mianlue suture zone on southern margin of Qinling-Dabie orogenic belt. *Sci. China Ser. D* **2004**, *47*, 300–316. [[CrossRef](#)]
32. Li, S.Z.; Kusky, T.M.; Wang, L.; Zhang, G.W.; Lai, S.C.; Liu, X.C.; Dong, S.W.; Zhao, G.C. Collision leading to multiple-stage large-scale extrusion in the Qinling orogen: Insights from the Mianlue suture. *Gondwana Res.* **2007**, *12*, 121–143. [[CrossRef](#)]
33. Yang, L.Q.; Deng, J.; Dilek, Y.; Qiu, K.F.; Ji, X.Z.; Li, N.; Taylor, R.D.; Yu, J.Y. Structure, geochronology, and petrogenesis of the Late Triassic Puziba granitoid dikes in the Mianlue suture zone, Qinling Orogen, China. *Geol. Soc. Am. Bull.* **2015**, *11/12*, 1831–1854. [[CrossRef](#)]
34. Wang, X.X.; Wang, T.; Zhang, C.L. Neoproterozoic, Paleozoic, and Mesozoic granitoid magmatism in the Qinling Orogen, China: Constraints on orogenic process. *J. Asian Earth Sci.* **2013**, *72*, 129–151. [[CrossRef](#)]
35. Li, N.; Chen, Y.J.; Santosh, M.; Pirajno, F. Compositional polarity of Triassic granitoids in the Qinling orogen, China: Implication for termination of the northernmost paleo-Tethys. *Gondwana Res.* **2015**, *27*, 244–257. [[CrossRef](#)]
36. Qiu, K.F.; Yu, H.C.; Gou, Z.Y.; Liang, Z.L.; Zhang, J.L.; Zhu, R. Nature and origin of Triassic igneous activity in the Western Qinling Orogen: The Wenquan composite pluton example. *Int. Geol. Rev.* **2018**, *60*, 242–266. [[CrossRef](#)]
37. Li, X.W.; Mo, X.X.; Huang, X.F.; Dong, G.C.; Yu, X.H.; Luo, M.F.; Liu, Y.B. U–Pb zircon geochronology, geochemical and Sr–Nd–Hf isotopic compositions of the Early Indosinian Tongren Pluton in West Qinling: Petrogenesis and geodynamic implications. *J. Asian Earth Sci.* **2015**, *97*, 38–50. [[CrossRef](#)]
38. Jin, W.J.; Zhang, Q.; He, D.F.; Jia, X.Q. SHRIMP dating of adakites in western Qinling and their implications. *Acta Petrol. Sin.* **2005**, *21*, 959–966, (In Chinese with English Abstract).
39. Luo, B.J.; Zhang, H.F.; Lü, X.B. U–Pb zircon dating, geochemical and Sr–Nd–Hf isotopic compositions of Early Indosinian intrusive rocks in West Qinling, central China: Petrogenesis and tectonic implications. *Contrib. Mineral. Petr.* **2012**, *164*, 551–569. [[CrossRef](#)]
40. Xu, X.Y.; Chen, J.; Gao, T.; Li, P.; Li, T. Granitoid magmatism and tectonic evolution in northern edge of the western Qinling terrane, NW China. *Acta Petrol. Sin.* **2014**, *30*, 371–389, (In Chinese with English Abstract).
41. Yu, H.C.; Guo, C.A.; Qiu, K.F.; McIntire, D.; Jiang, G.P.; Gou, Z.Y.; Geng, J.Z.; Pang, Y.; Zhu, R.; Li, N.B. Geochronological and Geochemical Constraints on the Formation of the Giant Zaozigou Au–Sb Deposit, West Qinling, China. *Minerals* **2019**, *9*, 37. [[CrossRef](#)]
42. Liu, C.X.; Li, L.; Sui, J.X. Mineralization Characteristics and Ore Genesis of the Zaozigou Gold Deposit, Gansu Province. *Geol. Sci. Tech. Inf.* **2011**, *30*, 66–74, (In Chinese with English Abstract).
43. Cao, X.F.; Sanogo, M.L.S.; Lv, X.B.; He, M.C.; Chen, C.; Zhu, J.; Tang, R.K.; Liu, Z.; Zhang, B. Ore-forming process of the Zaozigou gold deposit: Constraints from geological characteristics, gold occurrence and stable isotope compositions. *J. Jilin Univ. (Earth Sci. Ed.)* **2012**, *42*, 1039–1054, (In Chinese with English Abstract).
44. Zhang, X.H.; Ren, F.S.; Yu, C.; Liu, J.H.; Zhao, Y.Q.; Zhang, F.R.; Jia, Z.L. Breakthrough in geological prospecting based on study of metallogenic regularity. *Miner. Depos.* **2015**, *34*, 1130–1142, (In Chinese with English Abstract).
45. Luo, B.J. Petrogenesis and Geodynamic Processes of the Indosinian Magmatism in the West Qinling Orogenic Belt, Central China. Ph.D. Thesis, China University of Geosciences, Wuhan, China, 2013. (In Chinese)
46. Zhang, T.; Zhang, D.H.; Yang, B. SHRIMP zircon U–Pb dating of Gangcha intrusions in Qinghai and its geological significance. *Acta Petrol. Sin.* **2014**, *30*, 2739–2748, (In Chinese with English Abstract).
47. Huang, X.F.; Mo, X.X.; Yu, X.H.; Li, X.W.; Yang, M.C.; Luo, M.F.; He, W.Y.; Yu, J.C. Origin and geodynamic settings of the Indosinian Sr/Y granitoids in the West Qinling: An example from the Shehaliji pluton in Tonren area. *Acta Petrol. Sin.* **2014**, *30*, 3255–3270, (In Chinese with English Abstract).
48. Wei, P. Petrogenesis and Tectonic Setting of the Indosinian Granites from Xiahe Area, West Qinling. Master’s Thesis, China University of Geosciences, Beijing, China, 2013. (In Chinese)
49. Zhang, D.X.; Cao, H.; Shu, Z.X.; Lu, A.H. Indosinian magmatism and tectonic setting of Xiahe–Hezuo area, western Qinling Mountains—Implications from the Dewulu quartz diorite and Laodou quartz dioritic porphyry. *Geol. China* **2015**, *42*, 1257–1273, (In Chinese with English Abstract).
50. Jin, X.Y.; Li, J.W.; Sui, J.X.; Wen, G.; Zhang, J.Y. Geochronological and geochemical constraints on the genesis and tectonic setting of Dewulu intrusive complex in Xiahe–Hezuo District of Western Qinling. *J. Earth Sci. Environ.* **2013**, *35*, 20–38, (In Chinese with English Abstract).

51. Wang, Y.G.; Chi, J.; Wei, X.J.; Bi, S.T.; Han, X.Q.; Dong, C.R.; Wang, L.R. *Geological Survey Report of the Jiademu Gold-Polymetallic Deposit, Hezuo Country, Gansu Province*; Investigation Report; Guangxi Geological Exploration Institute of China Chemical Geology and Mine Bureau: Nanning, China, 2017. (In Chinese)
52. Anderson, T. Correction of common lead in U–Pb analyses that do not report ^{204}Pb . *Chem. Geol.* **2002**, *192*, 59–79. [[CrossRef](#)]
53. Liu, Y.S.; Gao, S.; Hu, Z.C.; Gao, C.G.; Zong, K.Q.; Wang, D.B. Continental and oceanic crust recycling-induced melt–peridotite interactions in the Trans-North China Orogen: U–Pb dating, Hf isotopes and trace elements in zircons from mantle xenoliths. *J. Petrol.* **2010**, *51*, 537–571. [[CrossRef](#)]
54. Ludwig, K.R. Isoplot v. 3.0: A geochronological toolkit for Microsoft Excel. In *Berkeley Geochronology Center*; Special Publication: Berkeley, CA, USA, 2003; pp. 1–70.
55. Elhlou, S.; Belousova, E.; Griffin, W.L.; Pearson, N.J.; O'Reilly, S.Y. Trace element and isotopic composition of GJ–red zircon standard by laser ablation. *Geochim. Cosmochim. Acta* **2006**, *70*, A158–A158. [[CrossRef](#)]
56. Scherer, E.; Münker, C.; Mezger, K. Calibration of the lutetium–hafnium clock. *Science* **2001**, *293*, 683–687. [[CrossRef](#)] [[PubMed](#)]
57. Blichert-Toft, J.; Albarède, F. The Lu–Hf isotope geochemistry of chondrites and the evolution of the mantle–crust system. *Earth Planet. Sci. Lett.* **1997**, *148*, 243–258.
58. Vervoort, J.D.; Blichert-Toft, J. Evolution of the depleted mantle: Hf isotope evidence from juvenile rocks through time. *Geochim. Cosmochim. Acta* **1999**, *63*, 533–556. [[CrossRef](#)]
59. Nowell, G.M.; Kempton, P.D.; Noble, S.R.; Fitton, J.G.; Saunders, A.D.; Mahoney, J.J.; Taylor, R.N. High precision Hf isotope measurements of MORB and OIB by thermal ionisation mass spectrometry: Insights into the depleted mantle. *Chem. Geol.* **1998**, *149*, 211–233. [[CrossRef](#)]
60. Griffin, W.L.; Pearson, N.J.; Belousova, E.; Jackson, S.E.; Achterbegrh, E.V.; O'Reilly, S.Y.; Shee, S.R. The Hf isotope composition of cratonic mantle: LAM-MC-ICPMS analysis of zircon megacrysts in kimberlites. *Geochim. Cosmochim. Acta* **2000**, *64*, 133–147. [[CrossRef](#)]
61. Griffin, W.L.; Wang, X.; Jackson, S.E.; Pearson, N.J.; O'Reilly, S.Y.; Xu, X.; Zhou, X. Zircon chemistry and magma mixing, SE China: In-situ analysis of Hf isotopes, Tonglu and Pingtan igneous complexes. *Lithos* **2002**, *61*, 237–269. [[CrossRef](#)]
62. Corfu, F.; Hanchar, J.M.; Hoskin, P.W.O.; Kinny, P. Atlas of zircon textures. In *Mineralogical Society of America; Reviews in Mineralogy and Geochemistry*; Hanchar, J.M., Hoskin, P.W.O., Eds.; Zircon: Washington, DC, USA, 2003; pp. 469–500.
63. Belousova, E.A.; Griffin, W.L.; O'Reilly, S.Y. Zircon crystal morphology, trace element signatures and Hf isotope composition as a tool for petrogenetic modelling: Examples from Eastern Australian granitoids. *J. Petrol.* **2006**, *47*, 329–353. [[CrossRef](#)]
64. Kemp, A.I.S.; Hawkesworth, C.J.; Foster, G.L.; Paterson, B.A.; Woodhead, J.D.; Hergt, J.M.; Gray, C.M.; Whitehouse, M.J. Magmatic and crustal differentiation history of granitic rocks from Hf–O isotopes in zircon. *Science* **2007**, *315*, 980–983. [[CrossRef](#)]
65. Zhu, D.C.; Mo, X.X.; Wang, L.Q.; Zhao, Z.D.; Niu, Y.L.; Zhou, C.Y.; Yang, Y.H. Petrogenesis of highly fractionated I-type granites in the Chayu area of eastern Gangdese, Tibet: Constraints from zircon U–Pb geochronology, geochemistry and Sr–Nd–Hf isotopes. *Sci. China Ser. D* **2009**, *52*, 1223–1239, (In Chinese with English Abstract). [[CrossRef](#)]
66. Yang, L.Q.; Deng, J.; Qiu, K.F.; Ji, X.Z.; Santosh, M.; Song, K.R.; Song, Y.H.; Geng, J.Z.; Zhang, C.; Hua, B. Magma mixing and crust–mantle interaction in the Triassic monzogranites of Bikou Terrane, central China: Constraints from petrology, geochemistry, and zircon U–Pb–Hf isotopic systematics. *J. Asian Earth Sci.* **2015**, *98*, 320–341. [[CrossRef](#)]
67. Huang, X.; Mo, X.X.; Yu, X. Middle Triassic magma mixing in an active continental margin: Evidence from mafic enclaves and host granites from the Dewulu pluton in West Qinling, central China. In *Proceedings of the American Geophysical Union Fall Meeting, San Francisco, CA, USA, 14–18 December 2015*.
68. Rapp, R.P.; Watson, E.B. Dehydration melting of metabasalt at 8–32 kbar: Implications for continental growth and crust–mantle recycling. *J. Petrol.* **1995**, *36*, 891–931. [[CrossRef](#)]

